JACS
JOURNAL OF THE AMERICAN CHEMICAL SOCIETY
Communication
pubs.acs.org/JACS

Synthesis of Stoichiometric FeS_2 through Plasma-Assisted Sulfurization of Fe_2O_3 Nanorods

Rachel Morrish, Rebecca Silverstein, and Colin A. Wolden*

Department of Chemical and Biological Engineering, Colorado School of Mines, Golden, Colorado 80401, United States

Supporting Information

ABSTRACT: Pyrite (FeS_2) thin films were synthesized using a H_2S plasma to sulfurize hematite (Fe_2O_3) nanorods deposited by chemical bath deposition. The high S activity within the plasma enabled a direct solid-state transformation between the two materials, bypassing S-deficient contaminant phases ($Fe_{1-x}S$). The application of plasma dramatically enhanced both the rate of conversion and the quality of the resulting material; stoichiometric FeS_2 was obtained at a moderate temperature of 400 °C using a chalcogen partial pressure $<6 \times 10^{-5}$ atm. As the S:Fe atomic ratio increased from 0 to 2.0, the apparent optical band gap dropped from 2.2 (hematite) to ∼1 eV (pyrite), with completely converted layers exhibiting absorption coefficients $>10^5$ cm^{-1} in the visible range. Room-temperature conductivity of FeS_2 films was on the order of 10^{-4} S cm^{-1} and approximately doubled under calibrated solar illumination.

Iron pyrite has come under renewed interest as a candidate for next-generation photovoltaics. In addition to being nontoxic and earth abundant, it has a remarkably large optical absorption coefficient ($>10^5$ cm^{-1}) and a modest band gap of ∼1 eV. Recent approaches to thin-film synthesis include the use of nanocrystal inks,[1,2] sulfurization of Fe[3,4] or Fe_2O_3[5,6] layers, and chemical vapor deposition (CVD).[7] Many of these techniques rely on exposure to elemental S vapor. Because S sublimes as a mixture of stable dimers and oligomers, it can be difficult to control. Berry et al.[7] recently reported that post-deposition S annealing was a critical step in converting their CVD-based films into pyrite and that the process was quite sensitive to both temperature and partial pressure. Detrimental effects of excess S exposure include pinhole formation, roughness, and subsequent condensation of bulk S on the surface. An alternative approach is exposure to H_2S, which offers precise and reproducible delivery of chalcogen through electronic mass flow control devices. However, H_2S still requires the use of elevated temperature, which can be problematic given pyrite's tendency to decompose at low temperature.[8] In this Communication we report the use of an inductively coupled plasma (ICP) source to activate H_2S to accelerate the conversion of hematite (Fe_2O_3) into stoichiometric FeS_2 films. In a plasma, high-energy electrons dissociate the feed gas into atoms, excited metastables (S*), and ions (S^+, S^-), enabling high reactivity. For example, the chemical potential of atomic S is ∼3 eV greater than that for H_2S. Such plasmas have previously been applied for converting In, Cu−In, and Cu−In−Ga to their respective chalcopyrite phases.[9]

We are aware of one previous report of subliming elemental S into an Ar plasma for conversion of iron films into pyrite, but the materials chemistry was not fully described.[10] One drawback of using elemental Fe as a precursor is that the transformation proceeds through intermediate $Fe_{1-x}S$ phases.[8,11] Diffusion of S through $Fe_{1-x}S$ is slow, making it a kinetically limited process, and complete elimination of the S-deficient phase could require additional processing steps.[8,11] Smedstad et al.[12] proposed the use of hematite as an alternative precursor. Their thermodynamic analysis suggested that hematite may be directly converted to pyrite, bypassing sub-stoichiometric phases, provided there is sufficiently high S activity. In this work, we describe the plasma-assisted H_2S sulfurization of hematite nanorods into FeS_2 films according to

$$Fe_2O_3 + 4H_2S \xrightarrow{\text{plasma}} 2FeS_2 + 3H_2O + H_2 \quad (1)$$

Fe_2O_3 nanorods grown on SnO_2:F-coated glass (FTO, Hartford Glass) by scalable chemical bath deposition were used as the starting hematite material. Nanostructured architectures have been proposed to address relatively short transport distances (∼100 nm) in pyrite while also supporting enhanced light harvesting and creating radial junctions for efficient carrier extraction. FTO also provides a convenient transparent contact for assessment of optoelectronic performance after sulfurization. Nanorods ∼150 nm long were grown from an aqueous bath of $FeCl_3$ and $NaNO_3$ as described previously.[13,14] The as-deposited FeOOH nanowires were calcined in air at 550 °C for 20 min to produce the hematite phase. Samples were then placed on a resistively heated stage just downstream of an ICP source used to activate a 10% H_2S:90% Ar mixture at 5.8×10^{-5} atm. A rf power of 80 W was applied, which was previously shown to be sufficient to dissociate nearly all the H_2S feed.[9] Further details on the exposure procedure are provided in the Supporting Information.

Figure 1 displays the evolution of S incorporation as a function of plasma exposure time at 400 °C. The S:Fe atomic ratio was measured using EDAX calibrated with a FeS_2 standard (Ted Pella); standardless quantification overestimated S composition. An accelerating voltage of 5 keV was adequate to survey the entire nanorod layer since the spectra included a significant Sn signal from the underlying substrate. Error bars represent 95% confidence intervals for three replicate samples. Within a given film, composition was typically uniform to ±3 at%. S incorporation was observed after just 1 min of H_2S plasma

Received: July 27, 2012
Published: October 15, 2012

   dx.doi.org/10.1021/ja307412e | J. Am. Chem. Soc. 2012, 134, 17854−17857

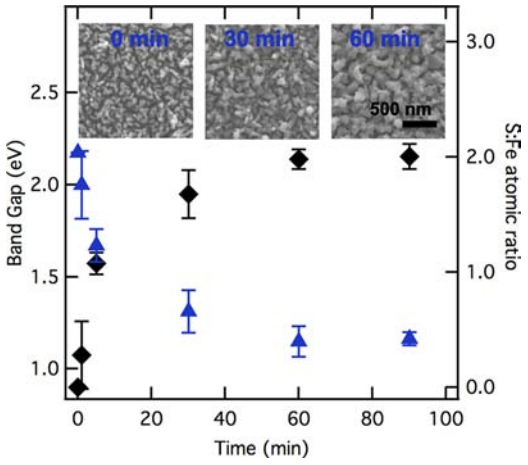

Figure 1. S:Fe ratio measured by calibrated EDAX (black diamonds) and corresponding direct optical band gap (blue triangles) for Fe_2O_3 sulfurization at 400 °C. Inset: FESEM images.

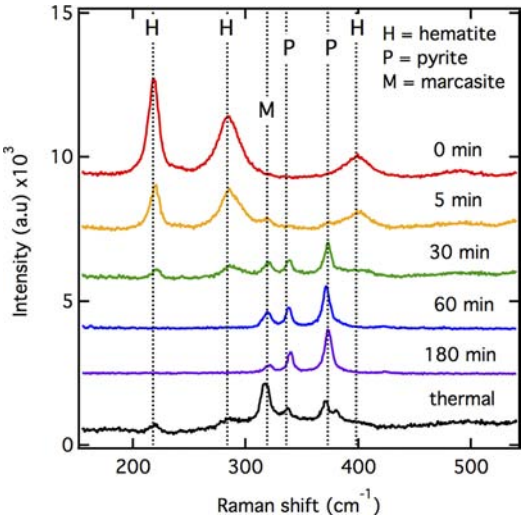

Figure 2. Raman spectra of Fe_2O_3 nanorods sulfurized at 400 °C.

exposure and increased until saturating with a S:Fe atomic ratio of 2.0 ± 0.02 at ∼60 min. The agreement with the expected FeS_2 stoichiometry supports a direct solid-state transformation of Fe_2O_3 to FeS_2, as clusters of residual $Fe_{1-x}S$ contaminates would depress the apparent S content. Notably, this complete conversion was achieved using a chalcogen feed pressure 4 orders of magnitude lower than typical requirements for thermal S vapor exposure.[4,7] Extended sulfurization times up to 8 h produced no further increase in the S:Fe atomic ratio, indicating an absence of elemental S buildup. Deleterious S condensation was not observed and may have been avoided due to the low chalcogen feed pressure in combination with the presence of atomic H released from H_2S, which could scavenge S contaminants. It is noted that exploratory investigations of sulfurization temperatures ranging from 350 to 450 °C found the quickest complete S incorporation was obtained at 400 °C. All data reported here were collected at this empirically optimum processing temperature.

Progressive FESEM images (Figure 1 inset) confirmed the surface retained a nanostructured architecture throughout the conversion, though the characteristic feature size approximately doubled from 50 to 100 nm. Magnified images of the films are given in Figure S1. Surfaces of samples exposed for >1 h showed no further changes, consistent with the composition measurements. The stable morphology suggests that the increase in feature size can be attributed to chemical effects of replacing, on average, 1.5 O atoms with 2 S atoms according to eq 1. Nanorod growth could also stem from localized heating due to atomic H recombination,[14,15] but such ripening would increase with time, and this was not observed.

As S was incorporated into the nanorod film, the direct optical band gap (determined from Tauc analysis) systematically decreased from 2.2 (hematite) to 1.2 eV (pyrite) (Figure 1). Indirect transitions could not be fit to samples reacted for <60 min but were consistently measured to be between 0.95 and 1.0 eV for fully converted films. When reported, direct transitions are often observed to be slightly wider in pyrite.[2,16,17] A more detailed discussion of the optical behavior follows presentation of wavelength-dependent absorption data in Figure 4, below.

The chemical transformation from Fe_2O_3 into FeS_2 was tracked using Raman spectroscopy (Figure 2). Raman is considerably more sensitive than X-ray diffraction (XRD) for distinguishing the pyrite and marcasite phases of FeS_2.[7] Samples were analyzed with a 532 nm diode laser configured to provide a resolution of <1 cm^{-1} over the region 150−550 cm^{-1}. The annealed Fe_2O_3 nanorods exhibited A_g bands at 218 cm^{-1} and E_g bands centered at 284 and 399 cm^{-1} (Figure 2, 0 min), consistent with hematite analyzed at laser intensities >3 mW, where reversible localized heating causes both broadening and a slight red shift in peak positions.[18]

After a 5 min exposure to the H_2S plasma at 400 °C, new peaks at 319, 336, and 373 cm^{-1} were observed (Figure 2, 5 min). The bands at 336 and 373 cm^{-1} match the E_g and A_g modes of pyrite, respectively.[19,20] Weak T_g peaks that nearly coincide with these primary pyrite shifts are also expected but cannot be resolved for polycrystalline films.[20] As sulfurization progressed, the intensity of the hematite signals decreased while the pyrite signals grew. After 60 min (Figure 2, 60 min) the hematite phase was no longer observed. This agrees well with the EDAX data (Figure 1) which showed a S:Fe stoichiometry of 2:1 following a 60 min reaction. Raman penetration depth, which can be approximated by α^{-1}, most certainly decreased as S was incorporated. In our most absorbing films, this corresponds to surveying the top 80 nm of the ∼150 nm thick nanorod layer.

The peak at 319 cm^{-1} is indicative of an A_g mode of marcasite, the orthorhombic polymorph of FeS_2.[19] Although tin disulfide (SnS_2), an expected product of the sulfurized FTO substrate, has a strong A_g shift in this region as well (312 cm^{-1}),[21] FeS_2 films prepared on bare glass exhibited a 319 cm^{-1} peak, confirming its assignment to marcasite. A second A_g mode of marcasite at 382 cm^{-1} appears as a shoulder on the dominant pyrite peak at 373 cm^{-1}. Marcasite has a band gap of 0.34 eV and is considered to be a contaminant within pyrite.[7,22] Extended reaction times reduced the fraction of marcasite within our films (Figure 2, 180 min) but could not completely eliminate it to the detection limit of Raman. Raman spectroscopy appears to be markedly sensitive to marcasite impurities, as XRD analysis of our films indicated phase-pure pyrite (Figure S2). Notably, the measured optical band gap of our FeS_2 films did not change appreciably as the marcasite fraction was reduced. Others have observed negligible impact on the electrical resistivity of pyrite films containing trace amounts of marcasite, and their influence on FeS_2 optoelectronic properties remains unclear.[7]

To assess the importance of applying a high S activity plasma for conversion, a control sample was exposed to the same partial pressure of H_2S at 400 °C for 4 h (Figure 2, thermal). In addition

dx.doi.org/10.1021/ja307412e | J. Am. Chem. Soc. 2012, 134, 17854−17857

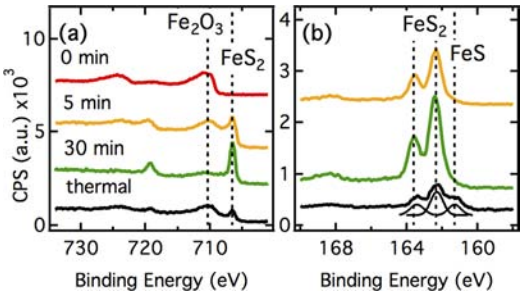

Figure 3. High-resolution XPS in the (a) Fe 2p and (b) S 2p regions of Fe_2O_3 nanorods sulfurized at 400 °C.

to the significant portion of hematite still remaining within the film (S:Fe = 1.20), the intensity of the marcasite peaks eclipsed those of pyrite. Others have found gas-phase sulfurization of Fe_2O_3 with H_2S to be slow.[5,23] In fact, Fe_2O_3 has been studied as a selective catalyst for gas-phase H_2S oxidation, implying its resistance to low-activity sulfurization.[24] Greater S pressures seem to favor formation of pyrite over marcasite,[7] which could explain the improved phase purity obtained with plasma-activated H_2S.

The surface chemistry of the sulfurized films was evaluated with XPS. Ar sputter cleans were not used because S is more readily etched than Fe, complicating surface analysis.[25] High-resolution spectra were collected at 40 eV pass energy and aligned on the basis of adventitious C 1s at 284.6 eV. Peaks were fit with a Shirley background and Voigt line shapes. Figure 3 shows spectra for the Fe 2p and S 2p regions. The starting hematite film (0 min) exhibited a primary $2p_{3/2}$ peak position of 710.3 eV, corresponding to fully oxidized Fe^{3+} with the associated satellite peaks.[26] After 5 min of H_2S plasma exposure, a peak at 706.5 eV appeared, matching Fe^{2+} in pyrite.[27] By 30 min, all evidence of superficial Fe_2O_3 had disappeared, replaced by FeS_2. High-resolution spectra of the S 2p region verified conversion to FeS_2, exhibiting only the expected spin-orbit-coupled $2p_{1/2}$ and $2p_{3/2}$ peaks at 163.6 and 162.4 eV, respectively (Δ = 1.2 eV).[27] Elemental S ($2p_{3/2}$ = 164.0 eV) was not detected in any of the H_2S-exposed films. S:Fe peak area ratios of completely converted FeS_2 surfaces ranged from 0.62 to 0.64, consistent with pyrite exposed to air.[27] The subtle broad peak at 169.5−167.5 eV can be attributed to ferric sulfates.[27]

While the thermally sulfurized sample did undergo partial conversion to FeS_2, it also contained a high fraction of FeS, shown by the additional S peak at 161.3 eV. Note that $Fe_{1-x}S$ species cannot be observed in Raman due to their structural symmetry.[20] Others have also observed formation of S-deficient phases during thermal H_2S exposure.[4] When reacting with gas-phase H_2S, Fe_2O_3 converts to FeS_2 by exchange of O^{2-} for S^{2-}.[23] Even at elevated temperatures, equilibrium decomposition of gas-phase H_2S is <10%, of which only a small fraction is the activated S ion.[28] Without sufficient S activity, thermal H_2S sulfurization proceeds through the intermediate $Fe_{1-x}S$ phase en route to FeS_2.[11] Conversely, application of a plasma results in >80% H_2S decomposition[9] and is clearly able to support a direct solid-state transformation. XRD data showed no evidence of crystalline S-deficient phases within the bulk of plasma-sulfurized films (Figure S2).

Pyrite's promise as a solar material is largely due to its favorable optical properties. Figure 4 shows the reflection corrected absorption coefficient, α, as hematite was converted to pyrite. Inset within Figure 4 is a direct band gap Tauc plot for Fe_2O_3 and

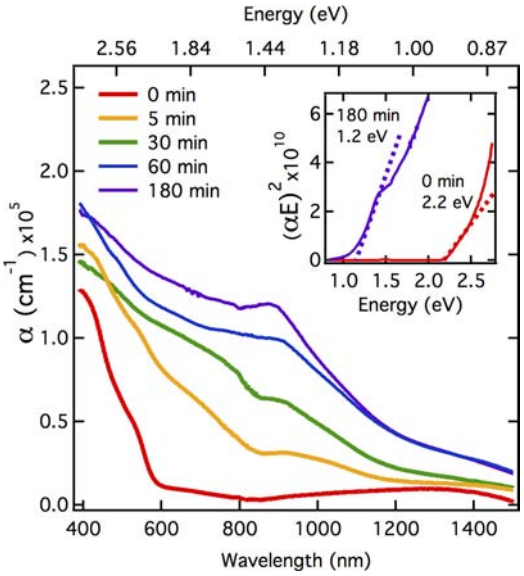

Figure 4. Absorption coefficient of Fe_2O_3 nanorods sulfurized at 400 °C. Inset: direct band gap Tauc plot for Fe_2O_3 and FeS_2 layers.

FeS_2 films. Fully converted FeS_2 layers exhibit a typical shape with $\alpha > 10^5$ cm^{-1} in the visible range. The soft band edge of FeS_2 compared to Fe_2O_3 could indicate a presence of defect states, though secondary transitions could not be identified from either direct or indirect Tauc analysis (Figure S3). Sulfurization beyond 60 min did not change the absorption onset or optical band gap but did show a slight increase in α below 1000 nm. Absolute values of α routinely varied by ±10% for replicate samples. This variation can be attributed to fluctuations in film thickness and local roughness, which influence the measured reflectance.

The gradual red shift of the absorption onset from just below 600 (0 min) to >1200 nm (60+ min) is not unlike trends observed in reverse type-1 heterostructures where a shell of low band gap material is overlaid on a wider gap material.[29,30] As shell thickness is increased, an outward shift of electrons and holes allows the band structure to be tuned.[30] This behavior is different than with two non-interacting planar layers, where primary transitions would be observed for each band gap so long as a significant fraction of light reaches the lower film. These heterostructures may serve as a reasonable model for H_2S plasma conversion of Fe_2O_3 to FeS_2. Because the surface reaction initiates on the top layer of material, directly transforming hematite to pyrite, incident light will travel through the narrower band gap FeS_2 first. As the reaction front progresses, the growing pyrite overlayer causes a systematic shift to higher wavelength absorption. Recent computational models have predicted that when pyrite is alloyed with O, light absorption will be greater than that with pyrite alone.[31] All films containing O in this work exhibited α values lower than stoichiometric FeS_2, which along with XPS further supports the direct transformation of hematite to pyrite without formation of intermediate alloys during plasma sulfurization.

Preliminary electrical characterization of fully sulfurized films was tested by evaporating Al dots on the surface to measure pyrite photoconductivity (Figure 5a). The current−voltage characteristics of pyrite produced by 90 min of plasma exposure are plotted in Figure 5b. The pyrite displays good ohmic behavior, and the dark conductivity was found to be 1.1×10^{-4} S cm^{-1}, which falls between recent reports of ~1 S cm^{-1} for highly pure, large-grain CVD films[7] and ~10^{-6} S cm^{-1} obtained from

dx.doi.org/10.1021/ja307412e | J. Am. Chem. Soc. 2012, 134, 17854−17857

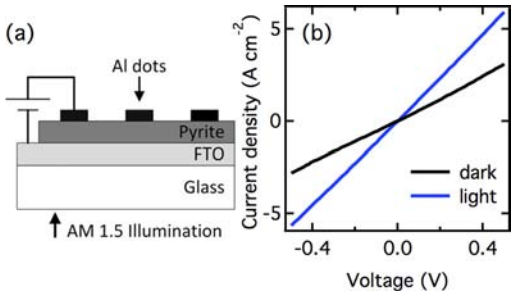

Figure 5. (a) Schematic of electrical measurements. (b) *I*–*V* characteristics of a 90 min sulfurized FeS_2 film.

dip-coated films assembled from pyrite nanocrystals.[2] Compilation of majority carrier properties from a range of natural and synthetic forms of pyrite has suggested maximum conductivities on the order of 1 S cm^{-1}.[32] The conductivity values reported scale with grain size, implying that control of this parameter and passivation of grain boundaries are critical to the achievement of high-quality solar absorbers. Samples were also tested when lit from the back side using a calibrated AM 1.5 light source. Upon illumination, the conductivity more than doubled to 2.3×10^{-4} S cm^{-1}. This photoresponse is comparable to other reports for nanocrystalline pyrite when evaluated under the same applied voltage.[2] Observation of measurable photoconductivity from a thin film does suggest promise for application of nanostructured pyrite as a solar absorber.

In summary, we have successfully applied H_2S plasmas to fully convert Fe_2O_3 nanorods into stoichiometric FeS_2. Contaminant $Fe_{1-x}S$ phases, which were readily detected during thermal processing, are absent in the plasma-assisted process. These findings substantiate thermodynamic models which predict a direct solid-state transformation between Fe_2O_3 and FeS_2 given sufficient sulfur activity. A combination of high reactivity at moderate conditions and fine control over chalcogen dosage implies this plasma sulfurization approach is not limited to the Fe–O–S system and could be utilized for conversion of more-sensitive metal oxides.

■ ASSOCIATED CONTENT

Ⓢ Supporting Information

Experimental details, high-magnification FESEM images, XRD data, and Tauc plots. This material is available free of charge via the Internet at http://pubs.acs.org.

■ AUTHOR INFORMATION

Corresponding Author

cwolden@mines.edu

Notes

The authors declare no competing financial interest.

■ ACKNOWLEDGMENTS

R.M. is grateful to the NSF for fellowship support under CHE-1137400. Additional funding provided by NSF DMR-1207294 and the Shared Research Program of the Center for Revolutionary Solar Photoconversion. We acknowledge Prof. Koh and the Center for Hydrate Research for use of their Raman spectrometer.

■ REFERENCES

(1) Puthussery, J.; Seefeld, S.; Berry, N.; Gibbs, M.; Law, M. *J. Am. Chem. Soc.* **2011**, *133*, 716.
(2) Bi, Y.; Yuan, Y. B.; Exstrom, C. L.; Darveau, S. A.; Huang, J. S. *Nano Lett.* **2011**, *11*, 4953.
(3) Soukup, R. J.; Prabukanthan, P.; Ianno, N. J.; Sarkar, A.; Kamler, C. A.; Sekora, D. G. *J. Vac. Sci. Technol. A* **2011**, 29.
(4) Caban-Acevedo, M.; Faber, M. S.; Tan, Y. Z.; Hamers, R. J.; Jin, S. *Nano Lett.* **2012**, *12*, 1977.
(5) Sunkara, M. K.; Pendyala, C.; Cummins, D.; Meduri, P.; Jasinski, J.; Kumar, V.; Russell, H. B.; Clark, E. L.; Kim, J. H. *J. Phys. D: Appl. Phys.* **2011**, *44*, 174032.
(6) Luan, Z. J.; Huang, L. Y.; Wang, F.; Meng, L. *Appl. Surf. Sci.* **2011**, *258*, 1505.
(7) Berry, N.; Cheng, M.; Perkins, C. L.; Limpinsel, M.; Hemminger, J. C.; Law, M. *Adv. Energy Mater.* **2012**, *2*, 1124.
(8) Yu, L.; Lany, S.; Kykyneshi, R.; Jieratum, V.; Ravichandran, R.; Pelatt, B.; Altschul, E.; Platt, H. A. S.; Wager, J. F.; Keszler, D. A.; Zunger, A. *Adv. Energy Mater.* **2011**, *1*, 748.
(9) Kosaraju, S.; Repins, I.; Wolden, C. A. *J. Vac. Sci. Technol. A* **2005**, *23*, 1202.
(10) Bausch, S.; Sailer, B.; Keppner, H.; Willeke, G.; Bucher, E.; Frommeyer, G. *Appl. Phys. Lett.* **1990**, *57*, 25.
(11) Ennaoui, A.; Fiechter, S.; Pettenkofer, C.; Alonsovante, N.; Buker, K.; Bronold, M.; Hopfner, C.; Tributsch, H. *Sol. Energy Mater. Sol. C* **1993**, *29*, 289.
(12) Smestad, G.; Ennaoui, A.; Fiechter, S.; Tributsch, H.; Hofmann, W. K.; Birkholz, M.; Kautek, W. *Solar Energ. Mater.* **1990**, *20*, 149.
(13) Vayssieres, L.; Beermann, N.; Lindquist, S. E.; Hagfeldt, A. *Chem. Mater.* **2001**, *12*, 233.
(14) Morrish, R.; Rahman, M.; MacElroy, J. M. D.; Wolden, C. A. *ChemSusChem* **2011**, *4*, 474.
(15) Wolden, C. A.; Mitra, S.; Gleason, K. K. *J. Appl. Phys.* **1992**, *72*, 3750.
(16) Lichtenberger, D.; Ellmer, K; Schieck, R.; Fiechter, S.; Tributsch, H. *Thin Solid Films* **1994**, *246*, 6.
(17) Kirkeminde, A.; Ruzicka, B. A.; Wang, R.; Puna, S.; Zhao, H.; Ren, S. *ACS Appl. Mater. Interfaces* **2012**, *4*, 1174.
(18) deFaria, D. L. A.; Silva, S. V.; deOliveira, M. T. *J. Raman Spectrosc.* **1997**, *28*, 873.
(19) Mernagh, T. P.; Trudu, A. G. *Chem. Geol.* **1993**, *103*, 113.
(20) Teo, M. Y. C.; Kulinich, S. A.; Plaksin, O. A.; Zhu, A. L. *J. Phys. Chem. A* **2010**, *114*, 4173.
(21) Price, L. S.; Parkin, I. P.; Hardy, A. M. E.; Clark, R. J. H.; Hibbert, T. G.; Molloy, K. C. *Chem. Mater.* **1999**, *11*, 1792.
(22) Wadia, C.; Wu, Y.; Gul, S.; Volkman, S. K.; Guo, J. H.; Alivisatos, A. P. *Chem. Mater.* **2009**, *21*, 2568.
(23) Davydov, A.; Chuang, K. T.; Sanger, A. R. *J. Phys. Chem. B* **1998**, *102*, 4745.
(24) Bukhtiyarova, G. A.; Delii, I. V.; Sakaeva, N. S.; Kaichev, V. V.; Plyasova, L. M.; Bukhtiyarov, V. I. *React. Kinet. Catal. Lett.* **2007**, *92*, 89.
(25) Hamdadou, N.; Khelil, A.; Bernede, J. C. *Mater. Chem. Phys.* **2003**, *78*, 591.
(26) Fujii, T.; de Groot, F. M. F.; Sawatzky, G. A.; Voogt, F. C.; Hibma, T.; Okada, K. *Phys. Rev. B* **1999**, *59*, 3195.
(27) Eggleston, C. M.; Ehrhardt, J. J.; Stumm, W. *Am. Mineral.* **1996**, *81*, 1036.
(28) Kaloidas, V. E.; Papayannakos, N. G. *Int. J. Hydrog. Energy* **1987**, *12*, 403.
(29) Zhong, X. H.; Xie, R. G.; Zhang, Y.; Basche, T.; Knoll, W. *Chem. Mater.* **2005**, *17*, 4038.
(30) Kim, S.; Shim, W.; Seo, H.; Bae, J. H.; Sung, J.; Choi, S. H.; Moon, W. K.; Lee, G.; Lee, B.; Kim, S. W. *Chem. Commun.* **2009**, 1267.
(31) Hu, J.; Z., Y.; Law, M.; Wu, R. *J. Am. Chem. Soc.* **2012**, *134*, 13216.
(32) Altermatt, P. P.; Kiesewetter, T.; Ellmer, K.; Tributsch, H. *Sol. Energy Mater. Sol. C* **2002**, *71*, 181.